Mon. Not. R. Astron. Soc. **369,** 416–424 (2006) doi:10.1111/j.1365-2966.2006.10325.x

High-resolution H I and radio continuum observations of the SNR G290.1−0.8

Estela M. Reynoso,[1,2]★† Simon Johnston,[3] Anne J. Green[2] and Bärbel S. Koribalski[3]

[1]*Instituto de Astronomía y Física del Espacio (IAFE), C.C. 67, Suc. 28, 1428 Buenos Aires, Argentina*
[2]*School of Physics, University of Sydney, NSW 2006, Australia*
[3]*Australia Telescope National Facility, CSIRO, PO Box 76, Epping, NSW 1710, Australia*

Accepted 2006 March 13. Received 2006 February 22

ABSTRACT

We have observed the supernova remnant (SNR) G290.1−0.8 in the 21-cm H I line and the 20-cm radio continuum using the Australia Telescope Compact Array (ATCA). The H I data were combined with data from the Southern Galactic Plane Survey to recover the shortest spatial frequencies. In contrast, H I absorption was analysed by filtering extended H I emission, with spatial frequencies shorter than 1.1 kλ. The low-resolution ATCA radio continuum image of the remnant shows considerable internal structure, resembling a network of filaments across its 13-arcmin diameter. A high-resolution ATCA radio continuum image was also constructed to study the small-scale structure in the SNR. It shows that there are no structures smaller than ∼17 arcsec, except perhaps for a bright knot to the south, which is probably an unrelated object. The H I absorption study shows that the gas distribution and kinematics in front of SNR G290.1−0.8 are complex. We estimate that the SNR probably lies in the Carina arm, at a distance 7 (±1) kpc. In addition, we have studied nearby sources in the observed field using archival multiwavelength data to determine their characteristics.

Key words: line: profiles – ISM: individual: G290.1−0.8 – supernova remnants – radio lines: ISM.

1 INTRODUCTION

The supernova remnant (SNR) G290.1−0.8 was originally discovered by Mills, Slee & Hill (1961) in their survey of radio sources and named MSH 11-6*1*A. It was first recognized as an SNR by Kesteven (1967). Based on observations at 408 MHz (Kesteven & Caswell 1987) and at 5 and 8 GHz (Milne et al. 1989), Green (1996) classified the remnant as shell type with an angular size of 15 × 10 arcmin^2, a flux density S of 40 Jy at 1 GHz, and a spectral index α ($S \propto \nu^{\alpha}$) of −0.4. Whiteoak & Green (1996) observed this SNR at 843 MHz with the Molonglo telescope and found considerable complex internal structure rather than the well-defined annular brightness distribution typical of shell SNRs.

Goss et al. (1972) observed the SNR in H I with a spectral resolution of 2 km s^{-1} using the Parkes radio telescope. Their spectrum shows H I emission in three broad peaks near −20, −10 and +25 km s^{-1}, appearing to extend to +50 km s^{-1}. From the absorption spectrum they assigned a lower distance limit of 3.6 kpc (the tangent point using the earlier model of $R_{\odot} = 10$ kpc) to the SNR. In a contemporary paper, Dickel (1973) claimed the SNR was *at* the tangent point but with little convincing evidence.

The optical counterpart to the radio SNR was discovered virtually simultaneously by Elliott & Malin (1979) and Kirshner & Winkler (1979). Both papers concluded that the remnant was much older and much further away than assumed by Dickel (1973) and estimated the distance to be 12–15 kpc. More recently, Rosado et al. (1996) studied the kinematics of G290.1−0.8 based on Hα observations and concluded that the kinematic velocity of the SNR is +12 km s^{-1}. However, the authors note the high complexity of the Hα emission along the line of sight to the remnant.

Seward (1990) detected the SNR in X-rays as part of his comprehensive survey of Galactic SNRs. Although the X-ray morphology shows some similarity to the radio shape, the emission is strongly peaked towards the centre. For this reason, Seward classifies the remnant as filled centre in contrast to the radio classification as a clumpy shell. Slane et al. (2002) analysed *Advanced Satellite for Cosmology and Astrophysics* (*ASCA*) observations of G290.1−0.8 and found that the X-ray emission is of thermal origin. Therefore, this remnant should be classified as a 'mixed-morphology' SNR, which are shell-like in radio wavelengths and centrally peaked in thermal X-ray emission (e.g. Rho & Petre 1998). With such a model, Slane et al. (2002) estimate that the distance to G290.1−0.8 must

★E-mail: ereynoso@iafe.uba.ar
†Member of the Carrera del Investigador Científico, CONICET, Argentina.

be in the range 8–11 kpc, while the age should be between 10 and 20 kyr.

Shaver & Goss (1970a,b) published images of the remnant at 408 and 5000 MHz in a field containing two other strong sources, G289.9−0.8 and G290.4−0.9. The first of these sources has a thermal spectrum and they classified the second as extragalactic based on its spectral index and the fact that it was unresolved using a 3-arcmin beam. Dickel & Milne (1972) classified G289.9−0.8 as an H II region based on a detection of a recombination line with a velocity of $+5\,\mathrm{km\,s^{-1}}$ and assigned a distance of 7.5 kpc to it. Grabelsky et al. (1988) observed a CO cloud at $l = 289\overset{\circ}{.}3$, $b = -0\overset{\circ}{.}6$ with a velocity of $+22\,\mathrm{km\,s^{-1}}$ to which they assign a distance of 7.9 kpc. Other H II regions in this vicinity have similar velocities and may be associated with the CO cloud. Grabelsky et al. (1988) comment that the SNR is 'seen close to a small CO peak'. *IRAS* and *Midcourse Space Experiment* (*MSX*) images in this region show the H II region G289.9−0.8 very clearly but little or no infrared emission is seen from the SNR. As seen in the Shaver & Goss (1970a) and the Grabelsky et al. (1988) images, there is an extended and complex region around $l = 290^\circ$ consisting of many H II regions and CO clouds which are clearly beyond the solar circle at a kinematic velocity of $22\,\mathrm{km\,s^{-1}}$. The SNR is located in the middle of this complex but there is no evidence of association.

Three pulsars lie in the vicinity of G290.1−0.8. Both PSR J1103−6025 (Kramer et al. 2003) and PSR J1104−6103 (Kaspi et al. 1996) have characteristic ages greater than 1 Myr and are located well outside the boundaries of the SNR. Of more interest is PSR J1105−6107 (Kaspi et al. 1997), a rapidly rotating pulsar with a characteristic age of only 63 kyr. Its dispersion measure is $271\,\mathrm{cm^{-3}\,pc}$, which implies a distance of 7 kpc, although the pulsar is located over two remnant radii away from SNR G290.1−0.8. Taking the age and distance at face value, and assuming the pulsar was born in the same event which produced the SNR, it would then need an average velocity of $\sim 700\,\mathrm{km\,s^{-1}}$ to reach the current position. This is high, although not impossible (e.g. Chatterjee et al. 2005). Slane et al. (2002) and Johnston & Weisberg (2006) suggest that PSR J1105−6107 is not likely to be associated with the remnant.

In this paper, we present new high-resolution H I line and 20-cm radio continuum observations towards G290.1−0.8 to understand more about this SNR and its environment.

2 OBSERVATIONS AND DATA REDUCTION

Simultaneous H I line and 20-cm radio continuum observations were carried out with the 1.5C and 750C configurations of the Australia Telescope Compact Array (ATCA) on 1995 May 16 and June 1, respectively. Both observations were of 14-h duration. With these configurations combined, there are 20 baselines ranging from 46 to 1480 m and an additional 10 baselines between 2000 and 5000 m. The phase centre was at (J2000) RA $= 11^{\mathrm{h}}\,03^{\mathrm{m}}\,24\overset{\mathrm{s}}{.}0$, Dec. $= -60^\circ 56' 11\overset{''}{.}0$. The primary beam has a full width at half-maximum (FWHM) of 33 arcmin at 1400 MHz. The H I measurements were centred at 1421 MHz using a 4-MHz bandwidth which was divided into 1024 channels. The velocity resolution is $1\,\mathrm{km\,s^{-1}}$. The radio continuum measurements were centred at 1384 MHz using a bandwidth of 128 MHz. The data reduction was carried out with the MIRIAD software package (Sault, Teuben & Wright 1995) using standard procedures. The primary flux and bandpass calibrator was PKS 1934−638, while PKS 1036−697 and PKS 1215−457 were used for phase calibration.

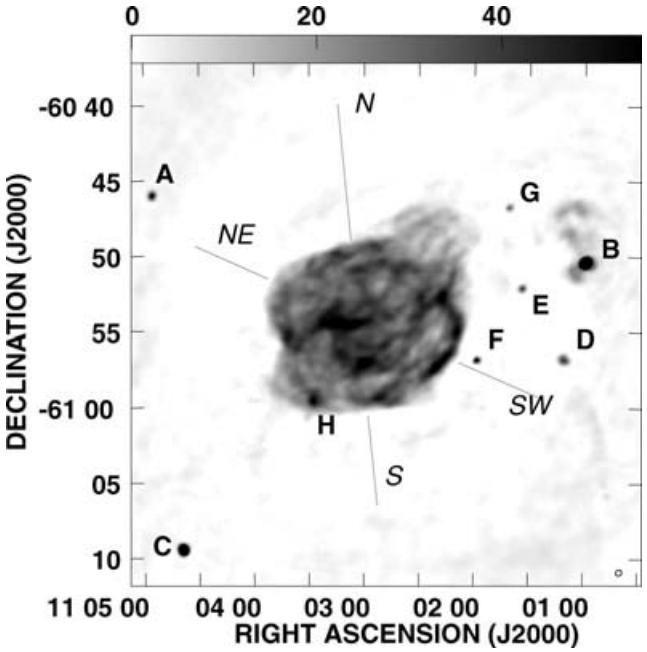

Figure 1. Radio continuum image of SNR G290.1−0.8 at 1384 MHz as obtained with the ATCA. The flux density scale, in units of mJy beam^{-1}, is displayed at the top of the image. The HPBW, $25.0 \times 22.5\,\mathrm{arcsec^2}$, PA $= -47^\circ$, is indicated in the bottom right corner. The rms noise level is $\sim$1 mJy beam^{-1}. Letters A–H indicate the compact sources discussed in the text. The two grey lines labelled as NE–SW and N–S (both interrupted at the SNR location) show the directions and extent of the two cuts in Fig. 2.

2.1 Radio continuum data

A low-resolution radio continuum image was constructed using all visibilities corresponding to baselines shorter than 1480 m. The data were Fourier transformed with 'uniform' weighting to minimize sidelobe levels. Compact sources were cleaned first, and then the residual image was used to find the clean components corresponding to diffuse emission. All clean components were finally convolved with a beam of $25 \times 23\,\mathrm{arcsec^2}$, with a position angle (PA) of -47°. The final image, shown in Fig. 1, has an rms noise level of $\sim$1 mJy beam^{-1}.

We also made a high-resolution image of this region using only the visibilities from 12.5 to 24 kλ (baselines from 2.6 to 5 km). In this u–v data set, structures larger than $\sim$17 arcsec are filtered out, and we find that virtually all the emission from the SNR is resolved out. All continuum images were corrected for the primary beam response.

Using the capability of ATCA to measure simultaneously continuum emission from two orthogonal linear polarizations, we constructed images of the Stokes parameters Q and U. No polarized emission was detected, and we do not discuss this further.

2.2 H I line data

To construct the H I cube, the continuum component was subtracted in the Fourier domain by fitting a linear baseline to 700 line-free channels. The data were Fourier transformed using 'natural' weighting, cleaned and restored with a synthesized beam of $58 \times 45\,\mathrm{arcsec^2}$, PA $= -86^\circ$. A sensitivity of $\sim$5 mJy beam^{-1} was achieved in line-free channels. To recover structures at shorter spatial frequencies, the ATCA H I data were combined in the u–v

plane with data from the Southern Galactic Plane Survey (SGPS; McClure-Griffiths et al. 2005). The latter combines Parkes and ATCA H I observations. No tapering was applied to the lower resolution cube. The line-free channels from the combined H I data set have an rms of $\sim$2 K.

For the absorption study, a second H I cube was constructed using the method in Reynoso et al. (2004), which is described in detail in Dickey et al. (2003). In this second cube, the continuum was not subtracted and all baselines shorter than 1.1 kλ were removed. The result is that all H I structures larger than $\sim$3.5 arcmin are filtered out. Since the continuum emission from G290.1−0.8 is dominated by smooth, extended structures, much of the continuum flux is also filtered out. However, the H I absorption features can still be easily seen towards the brightest structures. To deconvolve the data, the compact features were cleaned out and a cube with the residuals was obtained. This cube was further cleaned in a second stage. All clean components were restored with a 25 × 23 arcsec^2 beam, with PA = -79°. A filtered continuum image was constructed by averaging several line-free channels in the cube, and this was used to weight the final data cube. Absorption spectra can be computed by dividing the spectrum by the square of the integrated continuum flux from the same region.

3 RESULTS

3.1 Radio continuum results

The 20-cm radio continuum image of G290.1−0.8 and the surrounding complex region is shown in Fig. 1. The SNR shows considerable internal structure. The high resolution and sensitivity achieved with the present observations reveal a network of filaments across the face of the remnant. The sharp southern and northern edges of the SNR are remarkably straight, suggesting that the shock front may have encountered a plane parallel density gradient. There is some evidence for a 'blow-out' of material towards the north-west (NW) and south-east (SE). The NW 'blow-out' ends in a fringe with faint threads oriented in the direction of the major axis of the SNR, while the other bulge ends in a thin, very faint tail $\sim$4-arcmin long extending to the south. This weak tail is also seen in the 843-MHz image (Whiteoak & Green 1996). The flux density of G290.1−0.8 is estimated to be 25 Jy, which is about 40 per cent lower than the predicted value based on measurements in other frequencies.

Although this SNR has been classified as shell type, there is no evidence of shell structure in the 20-cm radio continuum image (Fig. 1) except for a bright arc at the western rim. To show this, we plot in Fig. 2 the intensity along two cuts across the remnant. The directions of the cuts [north-east–south-west (NE–SW) and north–south (N–S)] are shown in Fig. 1. Both cuts show the profiles of multiple narrow filaments, perhaps evidence of internal shocks.

The seven strongest compact sources in the field (all with flux densities $\geqslant$30 mJy beam^{-1}) are labelled A–G in Fig. 1. Source H is a bright patch of emission projected on to the southern rim of the SNR. Its possible association with the remnant is discussed below. Sources B and D are both associated with extended continuum emission with total flux densities of 1050 and 100 mJy, respectively. The parameters for these sources are listed in Table 1. The first column corresponds to the label as given in Fig. 1. Some of these sources have been identified in set of identifications, measurement and bibliography for astronomical data (SIMBAD), and we have included these identifications in the second column of Table 1. To compute the coordinates (third and fourth columns) and flux density at 20 cm (fifth column), the sources have been fitted with two-dimensional Gaussians. For double sources (see discussion below), the coordinates of the brightest component derived using the high-resolution image are listed. The sixth column gives the computed spectral index. The last two entries (systemic velocity and kinematical distance) are discussed in Section 3.2.

To compute the spectral indices, we used an 843-MHz radio continuum image [half-power beamwidth (HPBW) of 52 × 45 arcsec^2] obtained from the Sydney University Molonglo Sky Survey (SUMSS; Bock, Large & Sadler 1999). The ATCA 20-cm radio continuum image was convolved to the same resolution as the Molonglo image, and fluxes at both frequencies were compared in such a way that the slope between them gives a measure of the spectral index (Turtle et al. 1962). The method requires that the two images to be compared are filtered for the same $u - v$ coverage (Gaensler et al. 1999). Although this condition was not rigorously fulfilled here, the method may be used to give a good approximation for structures smaller than a few arcmin.

The high-resolution image reveals that several of these sources are extended or double. Source A shows a secondary peak more than three beams to the north of the brightest component, with a flux lower by a factor of $\gtrsim$2. Source B is resolved, and only $\sim$18 arcsec away from its centre, there appears a secondary source one order of

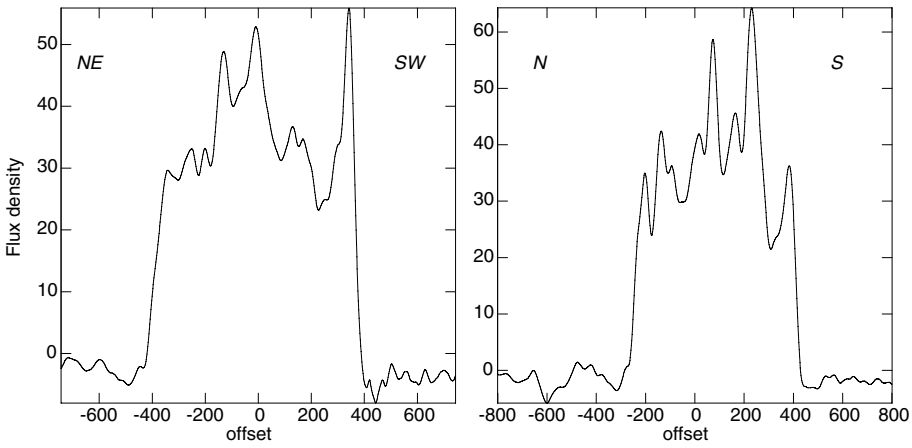

Figure 2. Two cuts across SNR G290.1−0.8 in the directions shown in Fig. 1 (NE–SW in the left-hand frame and N–S in the right). The flux density is given in mJy beam^{-1}, while the offsets are in arcsec and are referred to the central position in each cut.

Table 1. Parameters of the compact sources near SNR G290.1−0.8.

Source	Identification	Right ascension (J2000)	Declination (J2000)	Flux (mJy beam^{-1})	Spectral index	Systemic velocity (km s^{-1})	Kinematical distance (kpc)
A		$11^h04^m55^s$	$-60°45'58''$	77	-1.1 ± 0.1	$> +77$	>14
B	G289.8−0.8, *IRAS* 10588−6030, [CH87] 289.878−0.792, MSH 11−6*1*B	$11^h00^m59^s$	$-60°50'23''$	507	0.63 ± 0.08	(+20, +28)	(7.7, 8.4)
C		$11^h04^m39^s$	$-61°09'27''$	337	-0.85 ± 0.10	$> +115$	>20
D	G289.95−0.89, *IRAS* 10591−6040	$11^h01^m11^s$	$-60°56'49''$	82	0.0 ± 0.1	(+31.5, +70)	(8.8, 13)
E		$11^h01^m34^s$	$-60°53'08''$	35	-0.6 ± 0.2	$> +75$	>13
F		$11^h01^m58^s$	$-60°56'50''$	57	0.5 ± 0.1	$> +80$	>14
G		$11^h01^m41^s$	$-60°46'45''$	27	-0.7 ± 0.1	$> +75$	>13
H	MSX G290.2181−00.8153, *IRAS* 11014−6044	$11^h03^m28^s$	$-60°59'33''$	40	-0.4 ± 0.3	$> +80$	>14

magnitude fainter. Source C is resolved into two extended components separated by ∼45 arcsec, one of them being four times brighter that the other. Source H appears as a faint filament of size ∼16 × 4 arcsec^2 projected against the SNR. The two pulsars in the area were both detected. PSR J1104−6103's position is consistent with timing observations (Kaspi et al. 1996). There is a 4σ detection of the second pulsar, PSR J1105−6107.

We have also examined the 8.3-μm infrared image from the *MSX*,[1] shown overlaid on to our radio continuum image of G290.1−0.8 in Fig. 3. A few infrared point sources can be seen within the outermost contour of the SNR. The strongest of these (G290.1423−00.7577 in the MSX6C catalogue, or *IRAS* 11010−6038) is the infrared counterpart of the variable star dubbed as HD 95950 or V0 528 Car, with a spectral-type M2Iab. Source H lies slightly off-centre (by ∼5 arcsec) from an infrared source catalogued as MSX G290.2181−00.8153 and *IRAS* 11014−6044. The faint protrusion to the south of the SNR near H (see also Fig. 1), is found to be another unresolved source coincident with the infrared sources G290.2292−00.8311 (MSX6C catalogue) and IRAS 11014−6044.

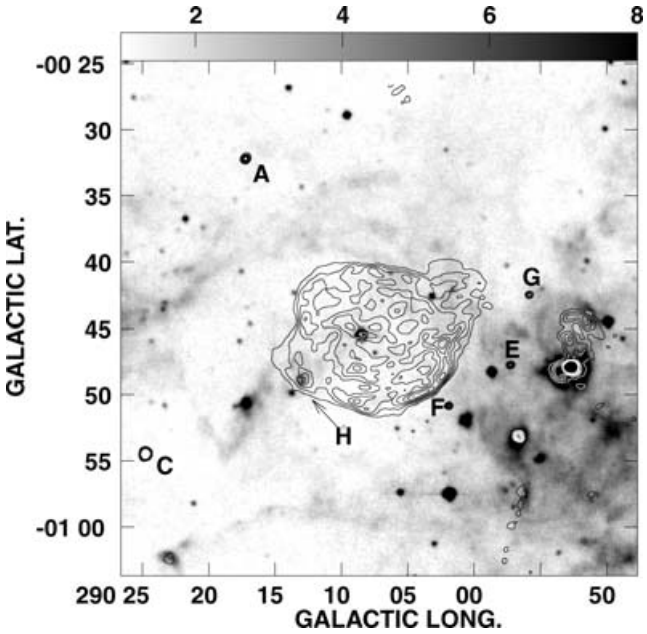

Figure 3. *MSX* infrared emission towards SNR G290.1−0.8 at 8.3 μm in grey-scale with 20-cm radio continuum contours overlaid. The grey-scale, in units of 10^{-6} W m^{-2} sr, is indicated at the top of the image. The contour levels range from 0 to 70 mJy beam^{-1}, in steps of 10 mJy beam^{-1}. For clarity, white contours are used over dark grey-scale background (e.g. sources B, D, H and IRAS 11010−6038 at the centre of the SNR). Source H (see Fig. 1) is indicated with an arrow. Labels have been included for sources A, C, E, F and G to avoid confusion between black radio contours and *MSX* emission.

3.2 H I results

The tangent point at $l = 290°$ is located at a distance of 2.9 kpc. According to the Galactic rotation model of Fich, Blitz & Stark (1989), there should be no H I gas with velocities more negative than -12 km s^{-1}. However, we observe H I emission to -30 km s^{-1}. Johnston et al. (1996) also detect departures in velocity from the Galactic rotation model of up to 20 km s^{-1} in this direction. The Carina spiral arm lies virtually along the line of sight at this longitude (Georgelin & Georgelin 1976), substantially affecting the gas velocities in this part of the Galaxy.

3.2.1 Compact sources

Spectra towards all sources (A–H) were obtained in both cubes in order to compare H I emission and absorption. All profiles are displayed in Fig. 4. The name of each source and their Galactic coordinates are indicated at the top of the H I emission profile, while the corresponding absorption profile is shown below. A brief description follows of the spectra for each of the sources.

Source A shows strong absorption up to +77 km s^{-1}, coincident with the most positive velocity emission feature, which implies a lower distance limit of 14 kpc. The steep spectral index indicates an extragalactic origin for this source.

Source B, named G289.9−0.8 by Shaver & Goss (1970b) and also known as MSH 11−6*1*B, shows strong absorption through all negative velocities and at +20 km s^{-1}. We assign source B a lower distance limit of 7.7 kpc and an upper limit of 8.4 kpc, the latter

[1] http://irsa.ipac.caltech.edu/applications/MSX/MSX/

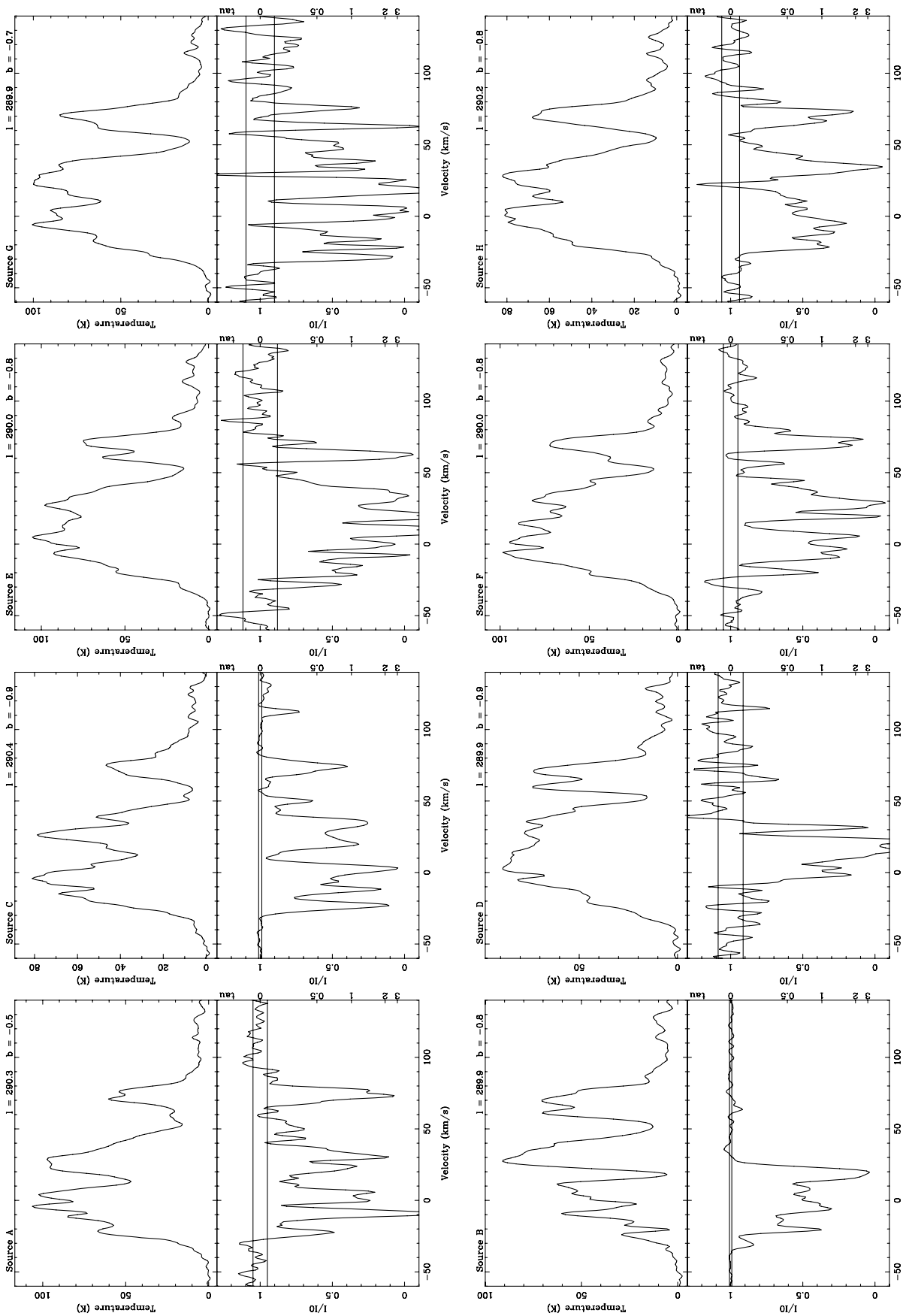

Figure 4. H I brightness temperature profiles (top) and absorption spectra (bottom) towards the compact sources in the field. The H I profiles, in K, are from the cube that combines Parkes and ATCA data. The absorption spectra and the corresponding emission profile, were computed as described in the text. In the absorption spectra, the vertical axis shows the ratio between the intensities at each velocity channel and the continuum (I/I_0, or $e^{-\tau}$) on the left and the opacity (τ) on the right. All profiles were Hanning smoothed. The name of each source and their Galactic coordinates are indicated at the top of each H I profile. The two horizontal lines close to $I/I_0 = 1$ show the 1σ noise level for each absorption profile. All velocities are with respect to the local standard of rest (LSR).

corresponding to $+28\,\mathrm{km\,s^{-1}}$, which is the first emission feature with no associated absorption. Bronfman, Nyman & May (1996) classify this source as an ultracompact H II region based on the detection of the CS 1-0 line at about $+20\,\mathrm{km\,s^{-1}}$. The extended source possibly associated with source B is very faint at 20 cm, which makes an absorption study difficult. From the H I data it is not possible to establish a physical link between the compact source B and the extended emission. The spectral index of the diffuse emission to the north of source B is 0.0 ± 0.1, typical of H II regions, while the spectral index of source B is $+0.63 \pm 0.08$, which is expected for stars with an ionized, uniform, spherically symmetric mass-loss flow (Wright & Barlow 1974).

Source C, shown as G290.4−0.9 on early radio images, shows strong absorption features to $+115\,\mathrm{km\,s^{-1}}$. This is the only source to clearly show absorption at such a high velocity. However, the brightness temperatures for the other sources in Table 1 are lower and any high-velocity absorption may be lost in the noise. The high-resolution image which shows that the source is a compact double and the steep spectral index strongly indicate that the source is extragalactic.

Sources D, E and F are all located within 6 arcmin of each other. The emission spectra in the direction of these sources are similar and yet D (the strongest of the three sources) shows a rather different absorption spectrum. Sources E and F clearly show absorption to $+33\,\mathrm{km\,s^{-1}}$ and again against the emission feature near $+70\,\mathrm{km\,s^{-1}}$, which implies lower distance limits of approximately 13 and 14 kpc, respectively. In contrast, source D shows no evidence for absorption against the $+70\,\mathrm{km\,s^{-1}}$ feature and is therefore likely to be a Galactic source. The lower distance limit to D is 8.8 kpc, based on the absorption feature at $+31.5\,\mathrm{km\,s^{-1}}$. Furthermore, it appears to be resolved in the visibilities measured for the longest baselines, recording only 25 per cent of the total intensity. Source D also has strong infrared emission and is coincident with a water–vapor maser (Scalise, Rodriguez & Mendoza-Torres 1989) located 8.9 kpc away, derived from a systemic velocity of $\sim +33\,\mathrm{km\,s^{-1}}$ from CS and $C^{34}S$ observations (Zinchenko, Mattila & Toriseva 1995).

Source G is the weakest point source listed. Its absorption spectrum is rather noisy and difficult to interpret. There appears to be absorption out to $+75\,\mathrm{km\,s^{-1}}$, implying a lower distance limit of ∼13 kpc. Finally, source H clearly shows absorption to $+80\,\mathrm{km\,s^{-1}}$, which sets a lower limit of 14 kpc for the distance. The range of possible velocities for each source according to the discussion above, and the derived distances, are summarized in the last two columns of Table 1.

3.2.2 *Supernova remnant*

To determine the kinematical distance to G290.1−0.8, we analysed absorption profiles towards different regions of the SNR, using the procedure described in Section 2.2. Pixels below 5σ, where $\sigma = 3\,\mathrm{mJy\,beam^{-1}}$, have been blanked. For each absorption spectrum, we produced 5σ envelopes to determine which features were significant. This method also filters out smooth scale continuum emission. From Fig. 5, where the resulting filtered continuum image is shown, it is seen that there are not many areas of the SNR where there is an opportunity to prepare absorption spectra using this method.

In Fig. 6, the two most convincing absorption profiles are displayed, towards the south and the west of the SNR (shown with boxes in Fig. 5). An average H I emission spectrum towards the whole area subtended by the SNR is included. The two absorption profiles look quite different: the western spectrum shows no

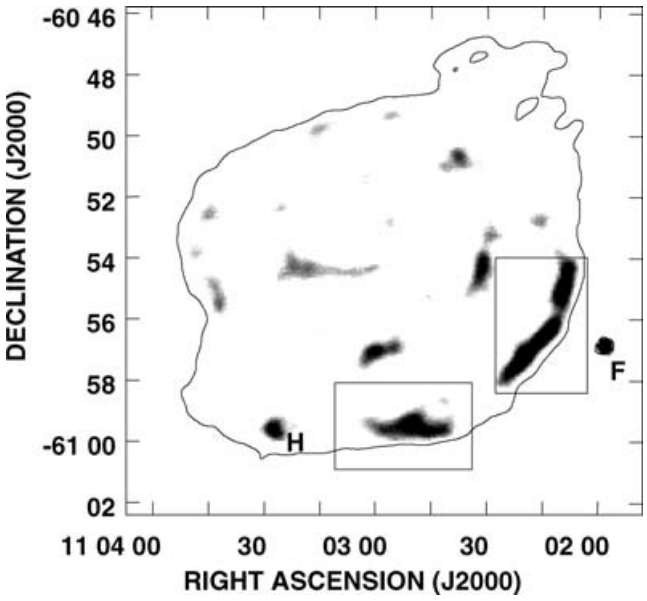

Figure 5. 20-cm radio continuum image of SNR G290.1−0.8 constructed by averaging several line-free channels of the filtered H I cube. Grey-scale shows the filtered intensity remaining after pixels below 5σ were blanked. The noise level is 3 mJy beam^{-1}. Boxes indicate the regions where H I absorption spectra are computed (south and west). The location of sources F and H are also indicated. A 20-cm radio contour at 1 mJy beam^{-1} is included.

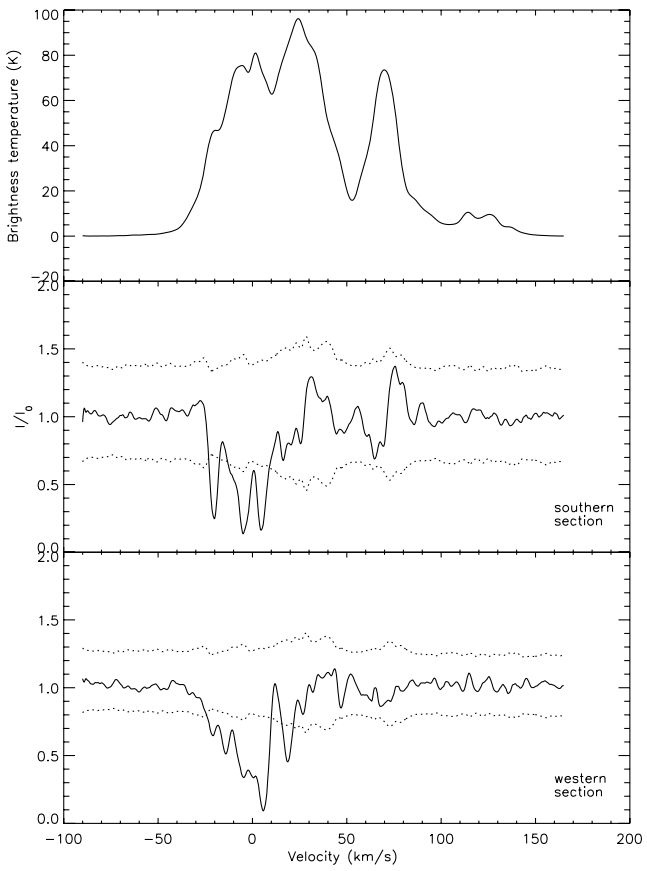

Figure 6. Upper frame: average H I emission profile towards SNR G290.1−0.8. Lower frames: H I absorption spectra towards two regions, to the south and to the west, as shown by the boxes in Fig. 5. The envelopes indicate 5σ uncertainties.

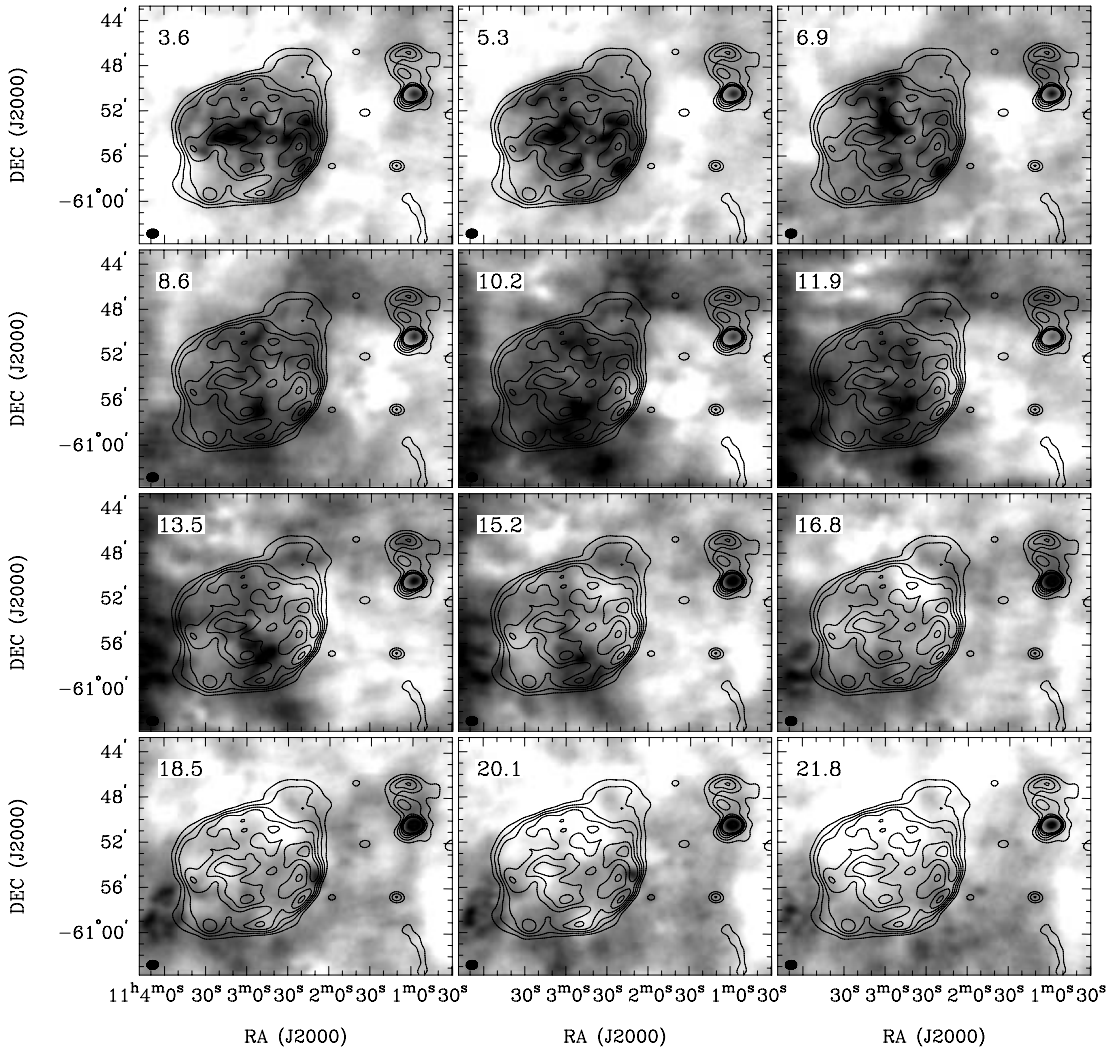

Figure 7. H I channel maps (grey-scale) of the ATCA + SGPS combined data cube covering SNR G290.1−0.8 and source B over the velocity range from +3.6 to +21.8 km s^{-1}, overlaid on the smoothed 20-cm radio continuum map (contours). The contour levels are 30, 70, 110, 150, 190, 230 mJy beam^{-1}. The grey-scale ranges from 40 (dark) to 100 K (bright). The beam (59 × 45 arcsec^2, PA = −86°) is displayed in the bottom left corner of each panel. For display purposes, we chose a channel width of 1.65 km s^{-1}, twice the original width. The H I velocities are indicated at the top left corner of each panel.

absorption beyond about +20 km s^{-1}, while the southern spectrum shows no absorption beyond about +7 km s^{-1}.

The interpretation of these H I spectra, particularly with respect to estimating the distance to the SNR, is complicated and described in the next section.

4 DISCUSSION

A visual inspection of the H I data cube shows that SNR G290.1−0.8 is seen unambiguously in absorption for velocities from −30 to approximately +7 km s^{-1}. Beyond this velocity the picture is not clear.

Fig. 7 shows images at 12 velocity channels from the H I cube to demonstrate the complexity of the structures and illustrate the difficulty in determining the systemic velocity for this SNR. H I absorption is clearly seen against most of the remnant out to velocities of about +7 km s^{-1}. The first channels displayed in Fig. 7 clearly show an 'H I shadow' within the outer contours of the radio continuum emission. We note that the H I emission and absorption across the face of the remnant vary substantially, with absorption structure that often does not correlate well with the continuum intensity peaks. Beyond about +7 km s^{-1} there is no obvious 'H I shadow' at the position of the remnant, partly due to diminished H I emission at velocities up to about +14 km s^{-1}. A slight drop in H I emission at the western edge of the remnant, at velocities around 18–20 km s^{-1}, is difficult to interpret, but most likely not due to absorption. In contrast, H I absorption against the very bright radio continuum emission of source B is clearly seen out to about +24 km s^{-1}.

The H I spectrum against the western rim (Fig. 6) shows a local minimum at +20 km s^{-1}. This is one of several features which are marginally above the 5σ detection limit. The feature does not appear in the H I spectrum against the southern rim. It is not possible to determine conclusively from the present data if this feature is associated with absorption by the SNR. If this velocity does represent the systemic velocity of the remnant, it would correspond to a distance of 7.7 ± 0.7 kpc.

Another anomaly complicating the interpretation of G290.1−0.8 concerns the bright compact source H which is located within the SNR rim. A comparison with the clearly unrelated source F is

helpful. Both sources are shown in Fig. 5. Inspection of the two absorption spectra (Fig. 4) shows obvious similarities, with strong positive velocity features at +33 and +70 km s^{-1}, indicating distances beyond the solar circle of more than 14 kpc. Source H also appears to have an infrared counterpart, catalogued in both the *IRAS* (11014−6044) and MSX (G290.2181−00.8153) surveys. Furthermore, the weak finger of continuum emission extending from source H, outside the SNR rim, also has an *MSX* source at the same position. Hence, it seems most likely that source H is unrelated to the SNR and the shock heated dust model to explain the *IRAS* spectrum (Junkes, Fürst & Reich 1992) has an origin not related to the formation of the SNR.

A common problem when studying H I absorption against a continuum source is confusion with self-absorption against the H I background. This happens when the optical depth along the line of sight is high and the phenomenon is typically seen as narrow features indicating the presence of small, cold clouds. For a small-scale object, an interferometer observes a brightness temperature $T_{\rm v} = T_{\rm s} - pT_{\rm g}$ (Schwarz et al. 1995), where $T_{\rm s}$ is the H I spin temperature, $T_{\rm g}$ is the background H I emission and p is the fraction of absorbed H I. To test the nature of the observed absorption, we followed the method employed by Schwarz et al. (1995) to determine the distance to Tycho's SNR: we plotted the minimum H I value per channel in the unfiltered interferometric cube towards the whole area subtended by G290.1−0.8, and towards regions away from the SNR in the four directions, north, south, east and west, all covering the same area. If features are similar on- and off-source, then self-absorption may be the explanation. The spectra are shown in Fig. 8. Clear absorption against the continuum emission from G290.1−0.8 is not found much beyond +7 km s^{-1}. The possibility of the +20 km s^{-1} feature being associated with the SNR is discussed previously. From Fig. 8, we can deduce that absorption is definitely associated out to +7 km s^{-1}, by observing the large differences between the SNR spectrum and the other spectra. For more positive velocities, we again see inconsistent results. Adopting a value of +7 km s^{-1} for the systemic velocity, the corresponding distance is about 7 ± 1 kpc, using the Fich et al. (1989) model for Galactic rotation. Note that the distance derived previously for +20 km s^{-1} is not greatly different from our proposed estimate and likely to be consistent within the uncertainties of the model and expected peculiar velocities.

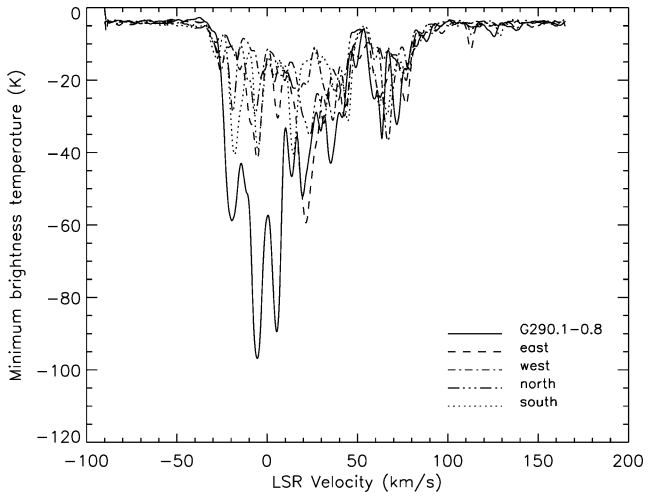

Figure 8. Spectra of the minima in the H I data as measured on the unfiltered ATCA data cube towards five regions of similar area: one over SNR G290.1−0.8, and four over the surroundings.

While the centrally peaked X-ray source is located near the central bright filament of the SNR, the distance estimate from the X-ray data of 8–11 kpc is not sufficiently well constrained to help us to determine the velocity range of features that are associated with absorption by the SNR. The column density measured by integrating the H I from the most negative velocity to the highest related positive velocity (taken as +10 km s^{-1}) is $N_{\rm H} = 4.5 \times 10^{22}$ cm^{-2}, which is not inconsistent with the value estimated by Slane et al. (2002) of 1.3×10^{22} cm^{-2}, given the uncertainties. The values would be even closer if the velocity of +20 km s^{-1} is adopted as the systemic velocity.

On balance, it seems likely that the systemic velocity is close to +10 km s^{-1}, which is in good agreement with the Hα result from Rosado et al. (1996) of +12 km s^{-1}, corresponding to a kinematic distance of ∼7 kpc. This places the SNR in the Carina arm with a linear diameter of about 25 pc at a scaleheight of nearly 100 pc, which are consistent with parameters for the known SNR population. The results from this work do present a consistent picture, notwithstanding the difficulty in interpreting the highly complex structure seen in H I data, which can be due not only to absorption by continuum sources, but real density variations, turbulence and velocity structure and self-absorption by cold clouds in the ISM.

The surface brightness of G290.1−0.8 is ∼3.5×10^{-20} W m^{-2} Hz^{-1} sr^{-1}. Statistically, high surface brightness SNRs (above 1×10^{-20} W m^{-2} Hz^{-1} sr^{-1}) are strongly concentrated around $l = 0°$, but there is another peak at $l = 290°$ (Green 2004). If this secondary peak is due to the fact that in this direction the Carina arm is crossed tangentially, and there is a concentration of high surface brightness SNRs in this arm, then it is very probably that G290.1−0.8 also belongs to the Carina arm. This is supporting evidence that G290.1−0.8 is at a distance of 7 kpc (systemic velocity ∼ +10 km s^{-1}).

5 CONCLUSIONS

We have imaged the SNR G290.1−0.8 in both the radio continuum and the 21-cm H I line using the ATCA. To recover the shortest spatial frequencies, our H I observations were combined with SGPS data (McClure-Griffiths et al. 2005). Absorption was analysed by filtering the H I data, keeping only the highest spatial frequencies (above 1.1 kλ).

In the 20-cm radio continuum image, G290.1−0.8 shows filamentary emission with little evidence of shell structure, although this SNR is classified as a shell type. The northern and southern edges of this SNR are remarkably straight, suggesting that the shock front may have encountered a plane parallel density gradient. However, no emission features with similar morphology were found in the H I cube at any velocity likely to be associated with G290.1−0.8.

The H I in this direction is very complex since the line of sight cuts tangentially through the Carina spiral arm. Departures in velocity of ∼20 km s^{-1} with respect to circular rotation model are common. To resolve the problem of the kinematic distance to G290.1−0.8, we made various tests and conclude that the upper limit of the systemic velocity is about +7 km s^{-1}, also in good agreement with the result obtained from Hα data (Rosado et al. 1996). This velocity is translated into a distance of 7 ± 1 kpc, in good agreement with the lower limit inferred from X-rays *ASCA* data (Slane et al. 2002).

Additionally, we studied eight radio sources in the field, including a compact knot in the southern rim of G290.1−0.8 which is probably an unrelated source. A high-resolution image constructed using only the baselines involving the sixth ATCA antenna (baselines from 2.6 to 5 km) revealed that some of these sources are

close doubles. Spectral indices were computed using the flux–flux method combining our observations with data from the SUMSS at 843 MHz. Distance limits were derived for all these sources based on their absorption spectra.

ACKNOWLEDGMENTS

The authors wish to thank Naomi McClure-Griffiths for her advices on the H I absorption analysis. This project was partially financed by grants ANPCyT-14018 and UBACYT A055 (Argentina). During part of this work, EMR was a visiting scholar at the University of Sydney. The ATCA is part of the Australia Telescope, which is funded by the Commonwealth of Australia for operation as a National Facility managed by CSIRO. This research has made use of the NASA/IPAC Infrared Science Archive, which is operated by the Jet Propulsion Laboratory, California Institute of Technology, under contract with the National Aeronautics and Space Administration.

REFERENCES

Bock D. C.-J., Large M. I., Sadler E. M., 1999, AJ, 117, 1578
Bronfman L., Nyman L.-Å., May J., 1996, A&AS, 115, 81
Chatterjee S. et al., 2005, ApJ, 630, L61
Dickel J. R., 1973, ApJ, 15, L61
Dickel J. R., Milne D. K., 1972, Aust. J. Phys., 25, 539
Dickey J. M., McClure-Griffiths N. M., Gaensler B. M., Green A. J., 2003, ApJ, 585, 801
Elliott K. H., Malin D. F., 1979, MNRAS, 186, 45
Fich M., Blitz L., Stark A. A., 1989, ApJ, 342, 272
Gaensler B. M., Brazier K. T. S., Manchester R. N., Johnston S., Green A. J., 1999, MNRAS, 305, 724
Georgelin Y. M., Georgelin Y. P., 1976, A&A, 49, 57
Goss W. M., Radhakrishnan V., Brooks J. W., Murray J. D., 1972, ApJS, 24, 123
Grabelsky D. A., Cohen R. S., Bronfman L., Thaddeus P., 1988, ApJ, 331, 181
Green D. A., 1996, in McCray R., Wang Z., eds, IAU Colloquium 145, Supernovae and Supernova Remnants. Cambridge Univ. Press, Cambridge, p. 419
Green D. A., 2004, Bull. Astron. Soc. India, 32, 335
Johnston S., Weisberg J. M., 2006, MNRAS, in press
Johnston S., Koribalski B., Weisberg J. M., Wilson W., 1996, MNRAS, 279, 661
Junkes N., Fürst E., Reich W., 1992, A&A, 261, 289
Kaspi V. M., Manchester R. N., Johnston S., Lyne A. G., D'Amico N., 1996, AJ, 111, 2028
Kaspi V. M., Bailes M., Manchester R. N., Stappers B. W., Sandhu J. S., Navarro J., D'Amico N., 1997, ApJ, 485, 820
Kesteven M. J. K., 1967, Aust. J. Phys., 21, 369
Kesteven M. J., Caswell J. L., 1987, A&A, 183, 118
Kirshner R. P., Winkler P. F., 1979, ApJ, 227, 853
Kramer M. et al., 2003, MNRAS, 342, 1299
McClure-Griffiths N. M., Dickey J. M., Gaensler B. M., Green A. J., Haverkorn M., Strasser S., 2005, ApJS, 158, 178
Mills B. Y., Slee O. B., Hill E. R., 1961, Aust. J. Phys., 14, 497
Milne D. K., Caswell J. L., Kesteven M. J., Haynes R. F., Roger R. S., 1989, Proc. Astron. Soc. Aust., 8, 187
Reynoso E. M., Green A. J., Johnston S., Goss W. M., Dubner G. M., Giacani E. B., 2004, Publ. Astron. Soc. Aust., 21, 82
Rho J., Petre R., 1998, ApJ, 503, L167
Rosado M., Ambrocio-Cruz P., Le Coarer E., Marcelin M., 1996, A&A, 315, 243
Sault R. J., Teuben P. J., Wright M. C. H., 1995, in Shaw R. A., Payne H. E., Hayes J. J. E., eds, ASP Conf. Ser. Vol. 77, Astronomical Data Analysis Software and Systems IV. Astron. Soc. Pac., San Francisco, p. 433
Scalise E., Jr, Rodriguez L. F., Mendoza-Torres E., 1989, A&A, 221, 105
Schwarz U. J., Goss W. M., Kalberla P. M., Benaglia P., 1995, A&A, 299, 193
Seward F. D., 1990, ApJS, 73, 781
Shaver P. A., Goss W. M., 1970a, Aust. J. Phys. Astrophys. Suppl., 14, 133
Shaver P. A., Goss W. M., 1970b, Aust. J. Phys. Astrophys. Suppl., 14, 77
Slane P., Smith R. K., Hughes J. P., Petre R., 2002, ApJ, 564, 284
Turtle A. J., Pugh J. F., Kenderdine S., Pauliny-Toth I. I. K., 1962, MNRAS, 124, 297
Whiteoak J. B. Z., Green A. J., 1996, A&AS, 118, 329
Wright A. E., Barlow M. J., 1974, MNRAS, 170, 41
Zinchenko I., Mattila K., Toriseva M., 1995, A&AS, 111, 95

This paper has been typeset from a TEX/LATEX file prepared by the author.